

Steam Degradation of Ytterbium Disilicate Environmental Barrier Coatings: Effect of Composition, Microstructure and Temperature

Tejero-Martin, D., Bai, M., Rincon Romero, A., Wellman, R. G. & Hussain, T.

Published PDF deposited in Coventry University's Repository

Original citation:

Tejero-Martin, D, Bai, M, Rincon Romero, A, Wellman, RG & Hussain, T 2022, 'Steam Degradation of Ytterbium Disilicate Environmental Barrier Coatings: Effect of Composition, Microstructure and Temperature', Journal of Thermal Spray Technology, vol. 2022.

<https://dx.doi.org/10.1007/s11666-022-01473-2>

DOI 10.1007/s11666-022-01473-2

ISSN 1059-9630

ESSN 1544-1016

Publisher: Springer

Open Access This article is licensed under a Creative Commons Attribution 4.0 International License, which permits use, sharing, adaptation, distribution and reproduction in any medium or format, as long as you give appropriate credit to the original author(s) and the source, provide a link to the Creative Commons licence, and indicate if changes were made. The images or other third party material in this article are included in the article's Creative Commons licence, unless indicated otherwise in a credit line to the material. If material is not included in the article's Creative Commons licence and your intended use is not permitted by statutory regulation or exceeds the permitted use, you will need to obtain permission directly from the copyright holder. To view a copy of this licence, visit <http://creativecommons.org/licenses/by/4.0/>.



Steam Degradation of Ytterbium Disilicate Environmental Barrier Coatings: Effect of Composition, Microstructure and Temperature

Daniel Tejero-Martin¹ · Mingwen Bai² · Acacio Rincon Romero¹ · Richard G. Wellman³ · Tanvir Hussain¹

Submitted: 30 May 2022 / in revised form: 22 September 2022 / Accepted: 22 September 2022
© The Author(s) 2022

Abstract Recession of environmental barrier coatings (EBC) in environments containing steam is a pressing concern that requires further research before their implementation in gas turbine engines can be realized. In this work, free-standing plasma-sprayed $\text{Yb}_2\text{Si}_2\text{O}_7$ coatings were exposed to flowing steam at 1350 and 1400 °C for 96 h. Three samples were investigated, one coating with a low porosity level ($< 3\%$) and 1 wt.% Al_2O_3 representing traditional EBCs porosity levels; and two coatings with higher porosity levels ($\sim 20\%$) representing abradable EBCs. Phase composition and microstructural evolution were studied in order to reveal the underlying mechanism for the interaction between high temperature steam and ytterbium disilicate. The results show depletion of Yb_2SiO_5 near the surface and formation of ytterbium garnet ($\text{Yb}_3\text{Al}_5\text{O}_{12}$) on top of all three coatings due to the reaction with gaseous Al-containing impurities coming from the alumina furnace tubes. The 1 wt.% Al_2O_3 added to the EBC sample exacerbated the formation of garnet at 1400 °C compared to the abradable samples, which presented lower quantities of garnet. Additionally, inter-splat boundaries were visible after exposure, indicating preferential ingress of gaseous Al-containing impurities through the splat boundaries.

Keywords environmental barrier coating · steam · ytterbium disilicate · thermal spray

Introduction

Nickel-based super-alloys have allowed the current generation of gas turbine engines for aerospace and energy generation to reach extraordinary levels of efficiency. Despite advances in protective coatings and active cooling, the service temperature is ultimately limited to the melting point of the nickel-based super-alloy substrate. SiC/SiC ceramic matrix composites (CMCs) have been identified as a suitable replacement as the material to be used in the hot section for the next generation of gas turbines. Their increased service temperature and superior strength/weight ratio at high temperatures compared to nickel-based super-alloys (Ref 1, 2) are regarded as the key to improving the performance and weight of future gas turbine engines.

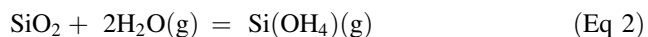
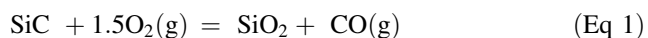
Before nickel-based super-alloys can be effectively replaced with CMCs (Ref 3), an effective and reliable protection against corrosion and degradation during service must be developed. CMCs exposed to service conditions face two main degradation mechanisms. Firstly, the presence of calcium magnesium alumina-silicates corrosive species (generally labeled as CMAS for convenience (Ref 4-6) can cause molten deposits that interact with the components, shortening their service life. CMAS can be present by the ingestion of debris during takeoff and landing, as well as when flying over arid environments or due to the presence of airborne volcanic ash (Ref 7, 8). Secondly, CMCs exposed to high temperatures under clean, dry oxygen form a protective SiO_2 scale that provides protection against corrosion and recession (Ref 9). Under the presence of steam, a naturally occurring combustion product (Ref 10, 11), the CMCs components show increased oxidation (Ref 12-14) and accelerated corrosion due to the volatilization of the SiO_2 scale to form gaseous Si-O-H species, such as $\text{Si}(\text{OH})_4$ (Ref 15), as shown below:

✉ Acacio Rincon Romero
acacio.rinconromero@nottingham.ac.uk

¹ Faculty of Engineering, University of Nottingham, University Park, Nottingham NG7 2RD, UK

² Institute for Future Transport and Cities, Coventry University, Priory St, Coventry CV1 5FB, UK

³ Surface Engineering, Rolls-Royce Plc, Derby DE24 8BJ, UK



This silica volatilization causes the recession of the surface of the component, which has been estimated to be as high as $\sim 1 \mu\text{m/h}$ under normal gas turbine operating conditions (Ref 16, 17). Since such components are expected to withstand at least 30,000 h of service without maintenance, this level of corrosion is unacceptable.

Environmental barrier coatings (EBCs) were then developed to negate the pernicious effects that CMAS and steam have on CMCs components (Ref 18). The current generation of EBCs generally presents a rare earth silicate top layer with a Si bond coat, providing direct protection against CMAS attack and silica volatilization. Several compositions have been suggested and studied (Ref 18), each one with its own set of advantages and disadvantages. Among those compositions, ytterbium disilicate (referred to as YbDS in this work) presents several promising characteristics. Its coefficient of thermal expansion is closely matched to that of SiC substrates ($3.6\text{--}4.5 \times 10^{-6} \text{ K}^{-1}$ for YbDS (Ref 19) and $4.5\text{--}5.5 \times 10^{-6} \text{ K}^{-1}$ for SiC (Ref 20)), it presents no phase transformation at high temperatures (Ref 21), adequate silica volatilization and low thermal conductivity at high temperatures ($\sim 2 \text{ W m/K}$ at $1000 \text{ }^\circ\text{C}$) (Ref 22).

Several studies have reported the interaction between heated steam and YbDS, although currently, there is no standard that allows easy and direct comparison. Additionally, the presence of alumina tubes in most testing rings influences the results through the presence of Al-containing contamination (Ref 23–26). Presentation of the YbDS testing material is varied, ranging from cold pressed pellets (Ref 24, 27), hot pressed pellets (Ref 28–30), coatings formed through oxidation bonded by reaction sintering (OBRS) (Ref 31), magnetron sputtering (Ref 32), dip coating (Ref 33) or coatings deposited using air plasma spraying (APS) (Ref 34, 35) or vacuum air plasma (Ref 36). Different deposition techniques result in differences in phase composition, microstructure, and porosity levels. Porosity, in particular, presents an interesting dilemma. Traditional EBCs aim for low levels of porosity to prevent steam reaching the substrate through connected pores; however, certain applications require higher levels of porosity. Abradable coatings, normally applied in the interior of the engine casing, for instance, are designed to present porosity as high as 20% in order to be eroded and allow the turbine blades to create a tight seal with the casing without risking damage due to friction (Ref 37). Despite the interest in abradable EBCs, no study has reported the effect that porosity has on the resistance to steam exposure of rare earth silicates.

In this work, three free-standing YbDS coatings deposited using air plasma spraying (APS), with three varying levels of porosity content, were studied. To evaluate the degree of degradation experienced, all three coatings were exposed to a flowing atmosphere of 90 vol.% $\text{H}_2\text{O}/10 \text{ vol.}\% \text{ O}_2$ with a flow velocity of $\sim 100 \text{ mm/s}$, atmospheric pressure and exposure time of 96 h. Two different tests were conducted, at 1350 and 1400 $^\circ\text{C}$, to investigate the effect that temperature has on the corrosion from steam with presence of gaseous Al-containing impurities. Temperatures and exposure duration were chosen in-line with OEM testing protocols and according to guidance from the high temperature community.

Experimental Methods

Materials and Steam Exposure

Three different free-standing YbDS coatings were studied in this work, one EBC coating with low levels of porosity manufactured to meet standard industrial requirements and two coatings with higher porosity levels representative of abradable EBCs, all of them produced using air plasma spraying using different custom powders to optimize the final coating microstructure. Free-standing coatings were achieved by spraying onto a steel bar without any grit blasting, then bending said bar to remove long, free-standing coatings. The standard environmental barrier coating, labeled in this work as EBC SG-100, which had a 1 wt.% of alumina powder added to the feedstock prior to spraying for increased fracture toughness (Ref 38). The coating was produced using Treibacher Industrie AG (Althofen, Austria) YbDS powder through a Praxair Surface Technology (Danbury, Connecticut, USA) SG-100 plasma spray gun. The abradable EBCs coatings were produced using YbDS powder that was provided by Oerlikon Metco AG (Pfäffikon, Freienbach, Switzerland), which is specifically designed for the production of abradable coatings. In addition, the YbDS feedstock powder was blended with a $\sim 1.5 \text{ wt.}\%$ of polyester powder prior to spraying. The polyester will act as a pore former that will lead to the desired porosity and abradable microstructure. The abradable coatings were deposited using two different guns, a Praxair Surface Technology SG-100 plasma spray gun, leading to a YbDS abradable coating labeled as ABR SG-100 (ABR is short for abradable), and an Oerlikon Metco F4 plasma spray gun, producing a YbDS abradable coating was labeled here as ABR F4. All the coatings were deposited by Rolls-Royce plc, using their proprietary deposition parameters. Both the Treibacher and Oerlikon YbDS powders were manufactured according to Rolls-Royce specifications. Powder

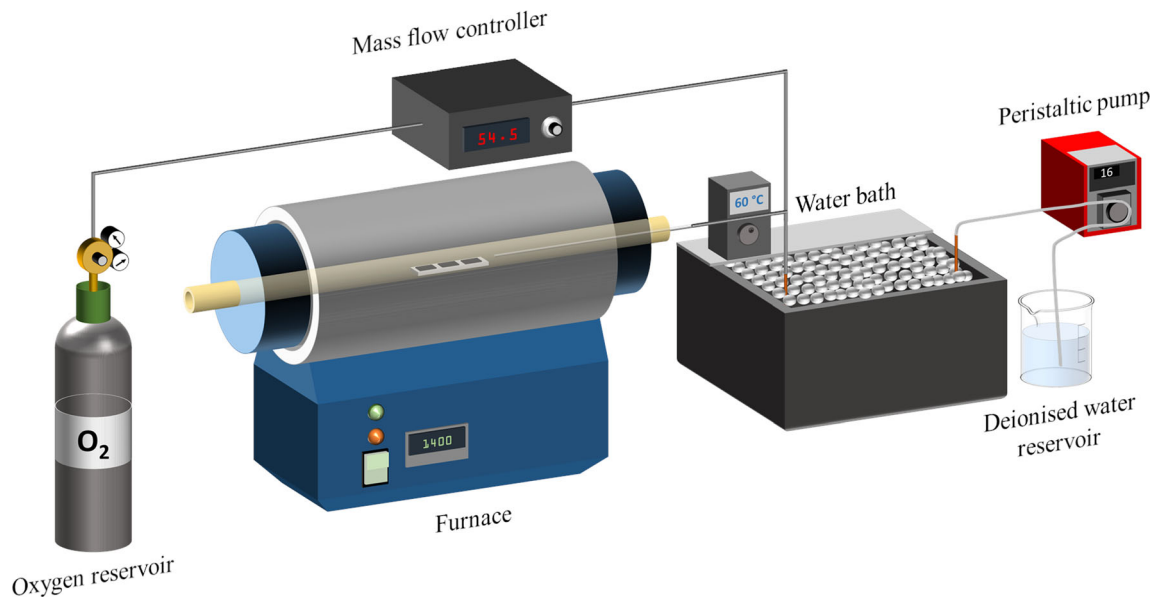


Fig. 1 Schematic of the custom steam rig designed and built for the steam exposure

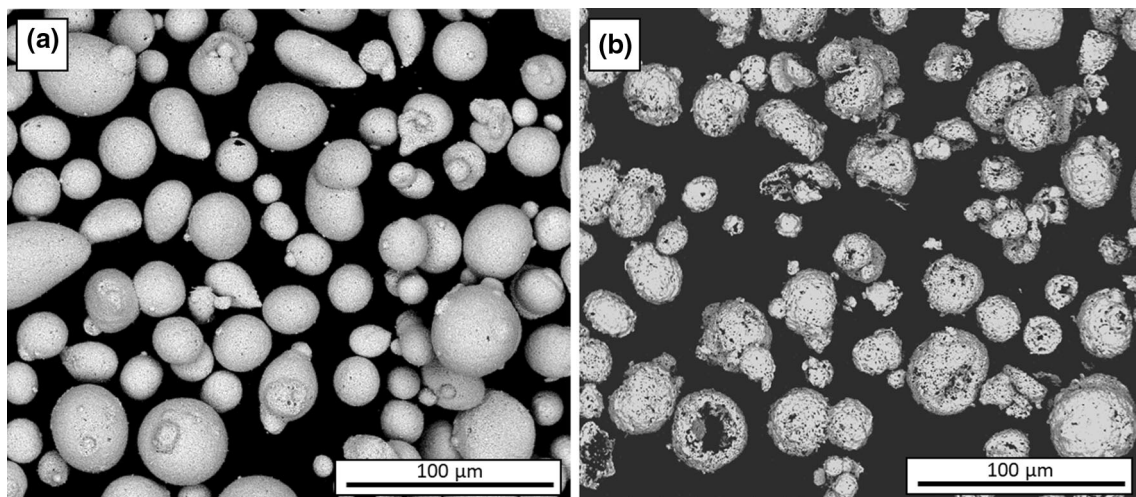


Fig. 2 BSE images of the powders used in this work: (a) corresponds to sample EBC, (b) corresponds to samples ABR

particle size was tailored to have a maximum of a 90 wt.% under $44\ \mu\text{m}$, with a composition having to conform to a nominal composition of 22–24 wt.% SiO_2 and balance of Yb_2O_3 , ytterbium monosilicate (YbMS) and SiO_2 . The focus in this paper was to investigate the microstructure-properties relationship; for this reason the spray parameters and powder compositions were selected to preserve the same ratio between YbDS and YbMS in all annealed samples and a porosity of around a 20% in the abrasible coatings. Microstructure and composition of all studied samples are in-line with commercial applications in future gas turbine engines. All three free-standing coatings were cut to produce samples with dimensions of $2.5 \times 1.5\ \text{cm}^2$. Previous

to any steam exposure, all of the free-standing as-sprayed samples were heat treated in order to crystallize the amorphous content. Free-standing samples were annealed at $1200\ \text{°C}$ for 2 h in air, with a heating and cooling rates of $5\ \text{°C}/\text{min}$.

Free-standing coatings were chosen for the test to eliminate the interaction with a Si bond coat and the substrate, aiming to investigate in detail the interaction between the steam and the YbDS layer.

For the steam exposure, a custom steam rig was designed and built, comprised of the different components shown in Fig. 1. The base of the steam rig is an Elite Thermal Systems Ltd (Market Harborough, UK) TSH15/25/180 tube furnace with an alumina tube with an internal

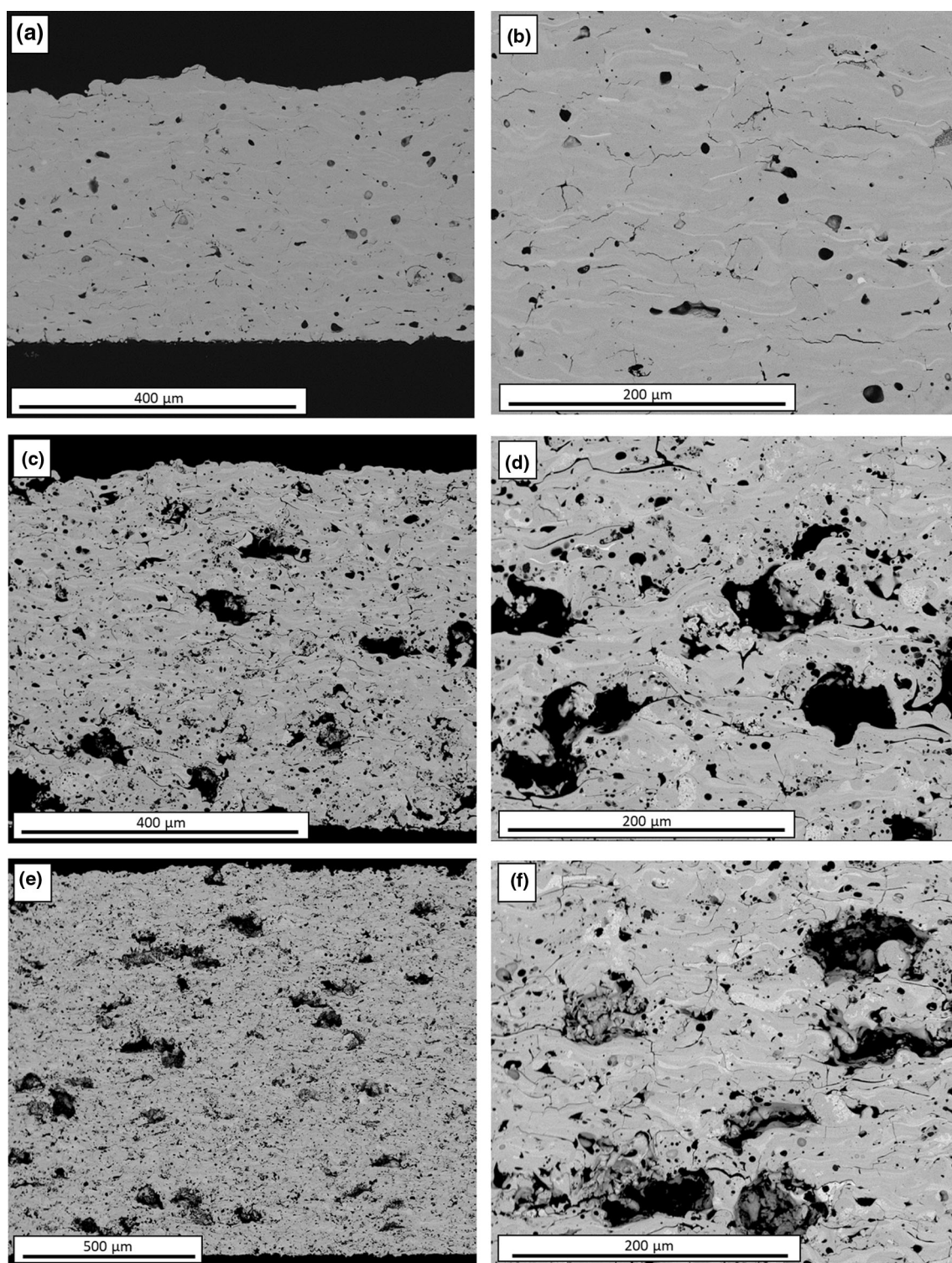


Fig. 3 BSE images of the three free-standing coatings after annealing at 1200 °C for 2 h. Images (a) and (b) show sample EBC SG-100, (c) and (d) ABR SG-100 and (e) and (f) ABR F4

diameter of 25 mm. An oxygen bottle is connected to one of the open ends of the tube, being the oxygen flow controlled with a MKS Instruments Inc. (Andover, Massachusetts, USA) type 247 mass flow controller. Deionized

water is introduced in the furnace via a Watson-Marlow (Falmouth, UK) 120S peristaltic pump with 0.63 mm bore PVC tubing. The deionized water is first passed through a Grant Instruments (Shepreth, UK) Optima TC120 heated

Table 1 Physical and mechanical properties of YbDS ceramic free-standing coatings.

Sample	Powder	Spray gun	Al ₂ O ₃ content, wt. %	Polyester content, wt. %	Thickness, μm	Porosity, %	Surface roughness, μm	Micro-hardness, Hv
EBC SG-100	Treibacher	Praxair SG-100	1	...	368 \pm 10	2.4 \pm 0.3	4.7 \pm 0.2	790 \pm 22
ABR SG-100	Treibacher	Praxair SG-100	...	1.5	509 \pm 9	21.3 \pm 1.1	1.8 \pm 0.2	431 \pm 29
ABR F4	Oerlikon Metco	Oerlikon Metco F4	...	1.5	1099 \pm 12	19.4 \pm 4.0	3.9 \pm 0.3	547 \pm 24

circulating bath kept at 60 °C to facilitate the evaporation once inside the furnace. Both the oxygen and water line are connected through a T connector outside the furnace, being the mixture introduced into the tube furnace using an alumina tube (99.7% purity) with an internal diameter of 1.5 mm, supplied by Almath Crucibles Ltd. (Newmarket, UK), reaching until the start of the hot zone. The other end of the tube furnace was kept open to maintain atmospheric pressure. Oxygen and water flow were set to obtain a flowing atmosphere at the hot zone with a content of 90 vol.% H₂O/10 vol.% O₂, and a gas velocity of \sim 100 mm/s. These parameters were chosen as they are similar to the H₂O partial pressure during lean hydrocarbon combustion at a pressure of 10 atm (Ref 39).

Oxygen and water flow were started once the furnace reached the desired temperature. Samples were placed on top of an alumina plate in the order shown in Fig. 1.

Two different exposures were conducted, the first one at 1350 °C and the second one at 1400 °C with a heating cooling rates of 10 °C/min, all the other parameters were kept constant between the two experiments. Testing temperatures were chosen to be in-line with the majority of the research done in the field. 1350 °C is a common temperature with coatings with a Si bond coat, as the Si melting point (\sim 1410 °C) is usually lowered by impurities. 1400 °C is another common study temperature, particularly if no Si bond coat is present. These two temperatures allow the coatings to be properly studied while allowing comparison with the current literature.

Material Characterization

Phase identification of the feedstock powder and free-standing coatings was performed using a Bruker D8 Advance Da Vinci diffractometer (Billerica, Massachusetts, USA) with Cu cathode (wavelength of 1.5406 Å) using Bragg–Brentano geometry. The angular range investigated was from 10° to 70° with a step size set to 0.02° and a dwell time of 0.3 s for all the measurements.

The sample holder rotated at 30 rpm during the data collection.

Quantitative Rietveld refinement (TOPAS V5, Bruker, Germany) was employed to determine the quantity of each phase the values are quantified in wt.% and the error is related to the mathematical error of the fitting (Ref 40). Surface roughness was measured using an optical profilometer Infinite Focus Advanced 3D System (Bruker Alicona, Austria) by measuring five profiles at different locations of the coating surface. The measurement reported represents the average and the standard error. To investigate the microstructure of the free-standing coatings, the samples were cold mounted using Struers EpoFix resin and hardener (Copenhagen, Denmark), then ground and polished to a 1 μm finish using Buehler SiC grinding papers (Leinfelden-Echterdingen, Germany). Micro-hardness was measured on the mounted coatings, using a Vickers micro-hardness Buehler indenter (USA) performing five measurements on each coating with a load of 300 gf and a dwell time of 10 s, being the value here reported the average micro-hardness.

Scanning electron microscope (SEM) images were taken using a FEI Europe Quanta 600 (Eindhoven, Netherlands). Porosity was calculated as the average measurement across three backscattered electron (BSE) images of representative regions of the coating. All the images were taken with a magnification of 400x, accelerating voltage of 15 kV and spot size of 5 nm. To do the porosity measurement, the open source software “ImageJ” with the image processing package “Fiji” was used (Ref 41). To do so, BSE images were converted into black and white maps upon setting a threshold. Then, the automated function “Analyze particle” was employed, which measured the area percentage of the image covered by porosity, returning an overall value per image. An average of the three images of each coating was calculated, being the standard deviation used as the error.

The thickness of the coatings and the width of YbMS depleted layer after steam exposure was evaluated in three backscattered images taken with the appropriate

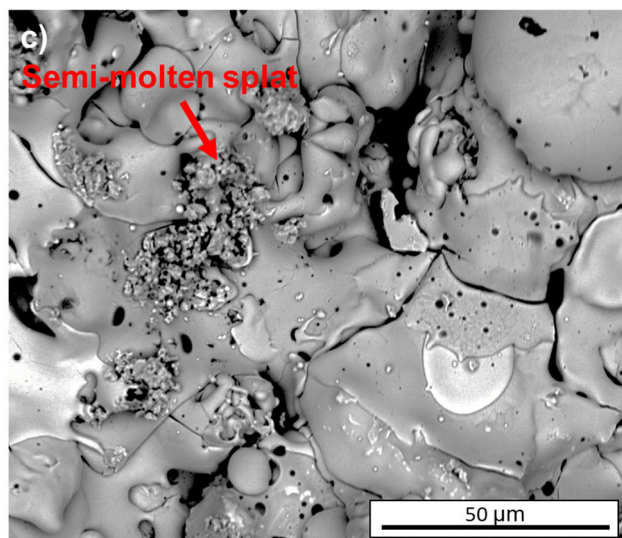
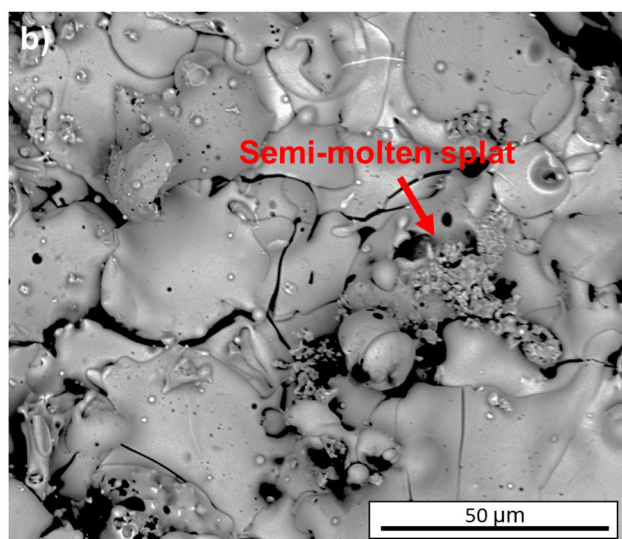
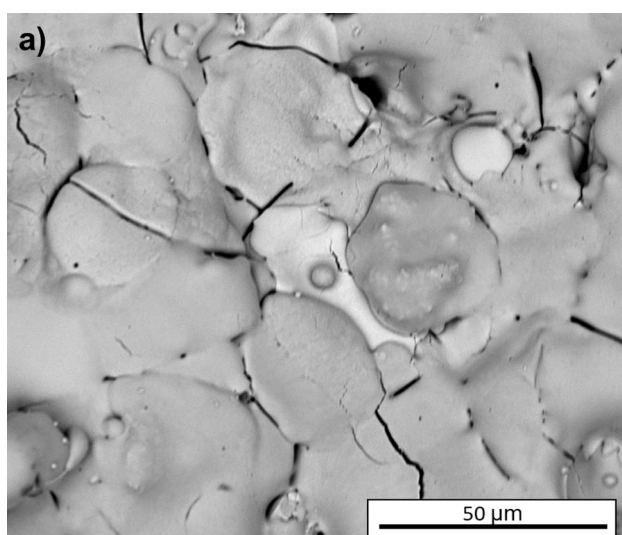
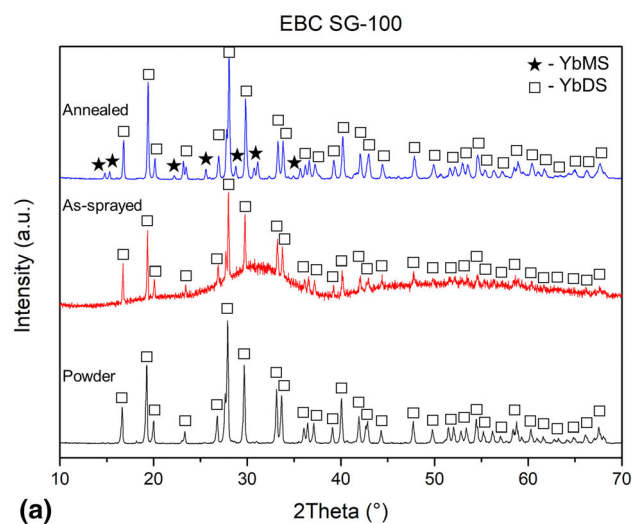
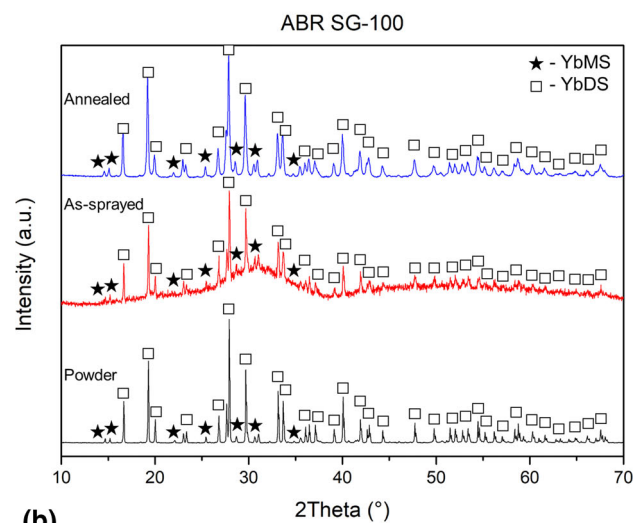


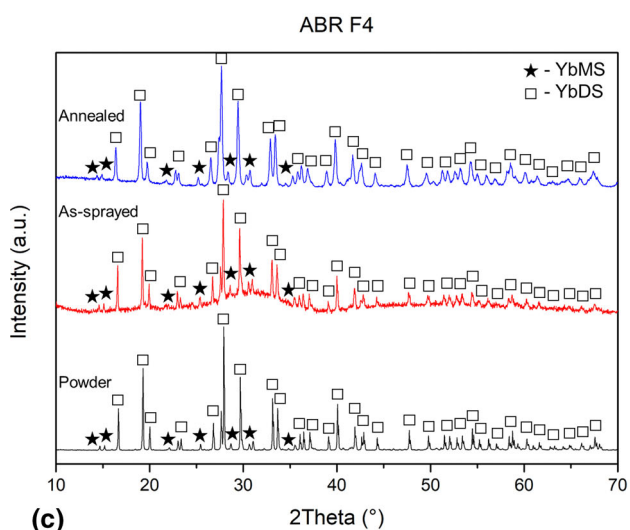
Fig. 4 BSE images of the top surface of the annealed samples (1200 °C for 2 h). Image (a) corresponds to sample EBC SG-100, image (b) to ABR SG-100 and image (c) to ABR F4



(a)



(b)



(c)

◀**Fig. 5** XRD measurements for (a) EBC SG-100, (b) ABR SG-100 and (c) ABR F4. On each graph, the bottom plot corresponds to the powder, middle to the as-sprayed coating and top to the annealed coating (1200 °C for 2 h). Phases have been identified with a star (★) for YbMS and a square (□) for YbDS

magnification, in order to evaluate the desired features and covering around 1 cm of the coating cross section with the different images. The reported data represents the average and standard error of nine measurements taken in that length.

EDS quantification of the coatings before and after steam exposure was conducted; however, the results (not shown here) were unreliable due to the small size of the studied features and the overlap between the Al-K_α (1.48 KeV) and Yb-M_α (1.51 KeV) energy lines.”

Results

Powder and Coating Characterization

Powder morphology was investigated through SEM imaging to better understand the microstructure of the produced coatings. Figure 2 shows a backscattered image of the two powders used in this study.

The morphology of the EBC powder, as shown in Fig. 2(a), is spherical in shape with a smooth surface, mostly lacking any defects or inclusion (Ref 42). On the other hand, ABR powder, as shown in Fig. 2(b), presents a more irregular shape, still mostly spherical, but with a rough surface and the presence of pores and visible hollow cores, which will enhance the production of micropores in the final coating.

In order to crystallize the amorphous content of the three as-sprayed coatings, they were annealed. Previous to any steam exposure, surface roughness of the three coatings was measured, providing values of $R_a = 4.7 \pm 0.2 \mu\text{m}$ for EBC SG-100, $R_a = 1.8 \pm 0.2 \mu\text{m}$ for ABR SG-100 and $R_a = 3.9 \pm 0.3 \mu\text{m}$ for ABR F4. Micro-hardness was measured as well, with values of $790 \pm 22 \text{ HV}$ for EBC SG-100, $431 \pm 29 \text{ HV}$ for ABR SG-100 and $547 \pm 24 \text{ HV}$ for ABR F4. The cross section of the annealed coatings are shown in Fig. 3.

The cross-sectional SEM images shown in Fig. 3 reveal that sample EBC SG-100 has a lower porosity level and thickness when compared to the two ABR coatings. This is confirmed by the porosity measurements, showing a porosity level of $2.4 \pm 0.3\%$ for EBC SG-100. On the other hand, sample ABR SG-100 has a porosity of $21.3 \pm 1.1\%$, and ABR F4 has $19.4 \pm 4.0\%$. The higher microporosity in the two ABR coatings is a direct

consequence of the hollow feedstock powder creating the micropores, whereas it is assumed that the macropores observed in the ABR SG-100 and ABR F4 samples are formed by the effect of the polyester particles (Ref 43). The polyester particles are embedded in the ceramic coating and, during the annealing, the polyester suffers thermal decomposition (350–500 °C) (Ref 44), leaving big empty pores behind. As for the thickness, measurements of sample EBC SG-100 revealed a thickness of $368.6 \pm 10.4 \mu\text{m}$, while ABR SG-100 was $509.9 \pm 9.2 \mu\text{m}$ and ABR F4 was $1099.7 \pm 12.7 \mu\text{m}$. The different thicknesses were chosen to represent the typical values required for each application in service, with EBCs traditionally remaining below 400 μm , whereas abrasable coatings are generally thicker. The physical and mechanical properties of the different samples are reported in Table 1.

The top surface of the annealed samples was investigated in an SEM to examine the morphology and provide a baseline to which exposed samples could be compared. The SEM images can be seen in Fig. 4.

From the images of the top surface shown in Fig. 4, it can be seen that sample EBC SG-100 presents a smooth surface with well-molten splats, along with cracks distributed across the surface. In the case of the two abrasable samples, ABR SG-100 and ABR F4, Fig. 4(b) and (c), respectively, the surface presents a combination of well-molten and semi-molten splats, the latter being labeled in the images.

The phase composition of the annealed coatings was also studied. The XRD diffractograms for the feedstock powder, as-sprayed and annealed conditions are shown in Fig. 5 for each of the three coatings.

The XRD measurements show that the EBC powder, Fig. 5(a), presents only peaks from the YbDS phase, $94.6 \pm 0.4 \text{ wt.}\%$ (PDF card number 00-082-0734), although Rietveld refinement identified a small quantity of YbMS ($5.4 \pm 0.4 \text{ wt.}\%$). The powder used to spray the abrasable samples, Fig. 5(b) and (c), shows the presence of a higher quantity of YbMS (PDF card number 00-040-0386), measured as $18.7 \pm 0.3 \text{ wt.}\%$. In the as-sprayed condition, EBC SG-100 only shows the presence of YbDS peaks with a 63.6 wt.% of amorphous content, whereas ABR SG-100 and ABR F4 present an amorphous phase in a 42.4% and a 57.1%. Samples ABR SG-100 and ABR F4 show YbMS peaks accounting for 24.7 ± 1.2 and $26.1 \pm 0.8 \text{ wt.}\%$, respectively. In addition to the crystalline peaks, all of the three as-sprayed coatings show two broad amorphous humps, centered on $\sim 30^\circ$ and $\sim 55^\circ$. The annealing process removes the presence of these amorphous humps, showing all of the three samples consist mainly of YbDS, with approximately $\sim 30 \text{ wt.}\%$ of YbMS. The detailed phase content as measured through Rietveld refinement is presented in Fig. 11.

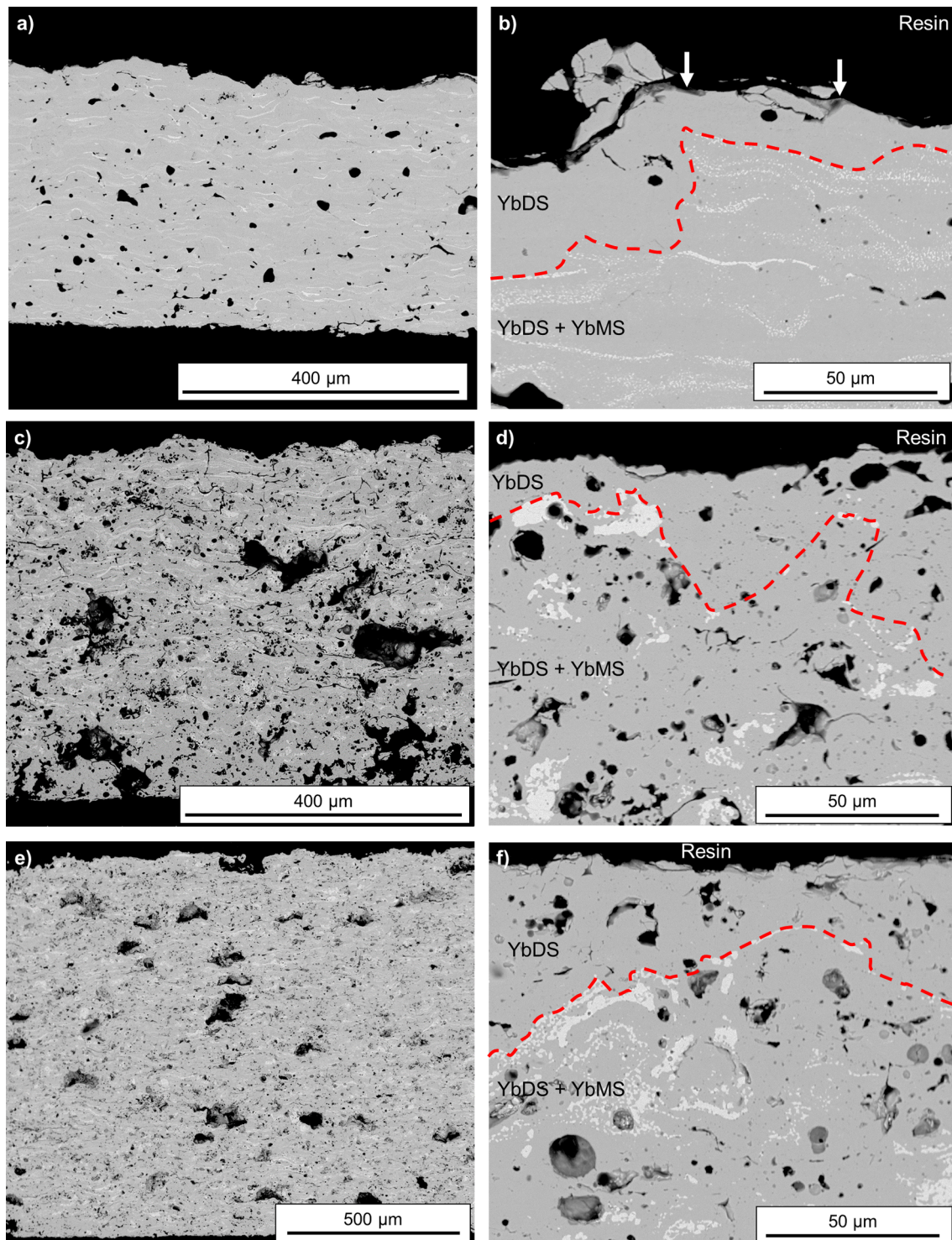


Fig. 6 Low and high magnification BSE images of the cross section of the samples exposed to steam for 96 h at 1350 °C. Images (a) and (b) correspond to sample EBC SG-100, images (c) and (d) to ABR

SG-100 and images (e) and (f) to ABR F4. The red dashed line marks where no more YbMS could be found. White arrows in image (b) indicate where a new phase was detected (Color figure online)

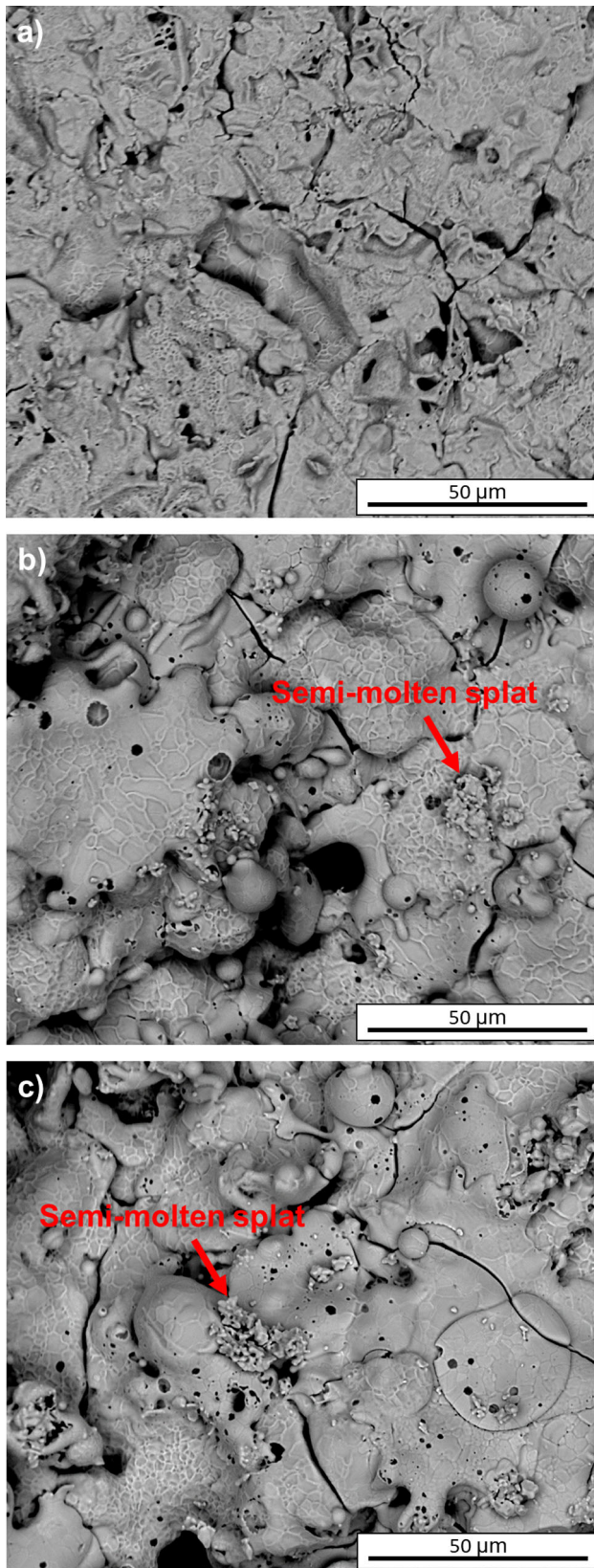


Fig. 7 BSE images of the top surface of the samples exposed to steam at 1350 °C for 96 h. Image (a) corresponds to sample EBC SG-100, image (b) to ABR SG-100 and image (c) to ABR F4

Steam Exposure at 1350 °C

The cross section of the samples exposed to steam at 1350 °C for 96 h is shown in Fig. 6.

From the SEM images shown in Fig. 6, it can be seen that exposure to steam at 1350 °C caused the depletion of the YbMS closest to the surface, leaving behind a YbMS depleted layer. The thickness of the depleted layer is $20 \pm 2 \mu\text{m}$ for the sample EBC SG-100, while ABR SG-100 and ABR F4 samples present a thickness of 45 ± 4 and $42 \pm 3 \mu\text{m}$, respectively. In the case of sample EBC SG-100, the high magnification image in Fig. 6(b) shows small amounts of a new phase (marked with arrows) present at the surface of the coating. Due to the size of these features and the overlap between the Al-K α and Yb-M α lines, EDS quantification was not reliable.

In addition to the cross section, the top surface of the exposed samples was also imaged. The images are shown in Fig. 7.

From the images of the top surface shown in Fig. 7, it can be seen that sample EBC SG-100, Fig. 7(a), has a smoother aspect, meaning the individual splats are more difficult to distinguish. On the other hand, samples ABR SG-100 and ABR F4, Fig. 7(b) and (c), still show the presence of individual splats, both molten and semi-molten. All of the three samples show the effects of steam exposure; the grain boundary attack on the splats is clearly visible. Multiple cracks, both intra- and inter-splat, are also visible on the three samples.

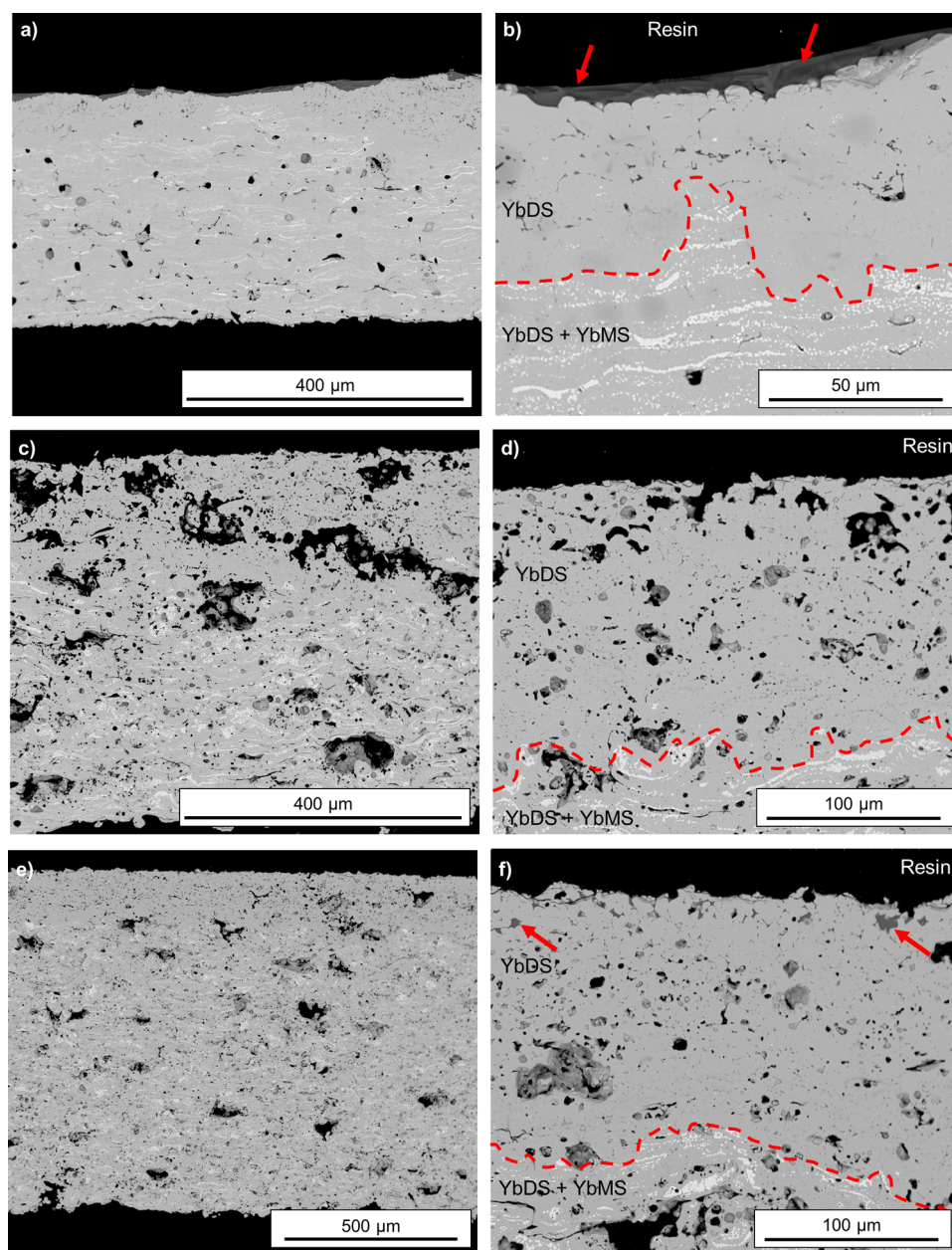
Steam Exposure at 1400 °C

SEM images of the cross section of the three coatings exposed to steam at 1400 °C for 96 h are presented in Fig. 8.

From the low and high magnification images of the three coatings exposed to steam at 1400 °C, as shown in Fig. 8, some differences can be appreciated. First, there is a clear new phase on the surface of sample EBC SG-100, marked with red arrows in Fig. 8(b). This scale, visible even at low magnification, was only present to such an extent on this sample. Smaller traces could be found within the coatings, especially in ABR F4, as marked with red arrows in Fig. 8(f). In the case of the abrasible samples, this new phase was not seen as a homogenous scale on top of the surface but as small patches and within filled pores. EDS identification was unreliable due to the already mentioned issue of overlapping peaks between the Al-K α and Yb-M α lines, so XRD analysis was used for identification, as shown in Fig. 10.

Another feature observed was the previously mentioned YbMS depleted layer near the surface of the coating. The thickness of the depleted layer in the case of sample EBC

Fig. 8 Low and high magnification BSE images of the cross section of the samples exposed to steam for 96 h at 1400 °C. Images (a) and (b) correspond to sample EBC SG-100, images (c) and (d) to ABR SG-100 and images (e) and (f) to ABR F4. The red dashed line marks where no more YbMS could be found. Red arrows in images (b) and (f) indicate where a new phase was detected (Color figure online)



SG-100 is $69 \pm 4 \mu\text{m}$, whereas the thickness of the depleted layer on the abrasable samples is thicker: $143 \pm 7 \mu\text{m}$ in sample ABR SG-100 and $151 \pm 5 \mu\text{m}$ for sample ABR F4. It should be noticed that steam recession is only observed in the coatings surface, not observing any microstructural or compositional changes in the bottom surface of the coatings. In addition, the top area of the depleted layer presents inter-splat boundaries, not present in the samples exposed to steam at 1350 °C, as it can be seen in Fig. 6. These newly formed features were located at the inter-splat boundaries and can be more clearly seen in sample EBC SG-100 due to the initial low level of

porosity. The top surface of the three coatings exposed to steam at 1400 °C was imaged, as shown in Fig. 9.

From the SEM images of the top surface, the grain boundary attack is less visible in the EBC SG-100 sample exposed to 1400 °C (Fig. 9a) compared to 1350 °C (Fig. 7a). Individual splats are difficult to identify, whereas cracks are visible. The top surface of the two abrasable coatings, ABR SG-100 (Fig. 9b) and ABR F4 (Fig. 9c), shows very similar features, with presence of semi-molten splats. Individual splats affected by grain boundary corrosion can be seen, as well as cracks.

XRD measurements were taken to study the phase content of the three coatings. Figure 10 shows the XRD

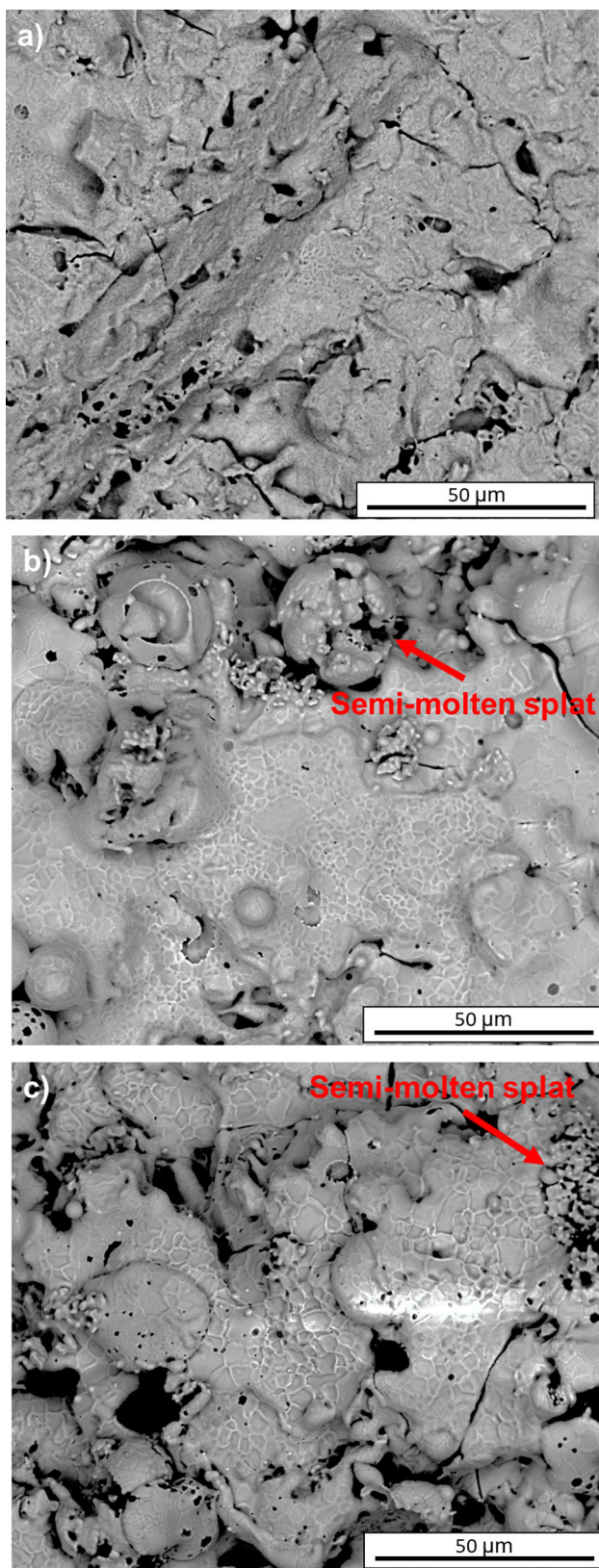


Fig. 9 BSE images of the top surface of the samples exposed to steam at 1400 °C for 96 h. Image (a) corresponds to sample EBC SG-100, image (b) to ABR SG-100 and image (c) to ABR F4

measurements of the three coatings on the three different conditions studied: before exposure, after exposure at 1350 °C and after exposure after 1400 °C.

The XRD measurements for sample EBC SG-100, Fig. 10(a), show how once the sample is exposed to steam at 1350 °C, there is a reduction in the intensity of the YbMS peaks. For EBC SG-100, this means a reduction from an YbMS content of 29.3 ± 0.4 wt.% down to 8.1 ± 0.4 wt.%, as shown in Fig. 11. In the case of the two abrasible samples, ABR SG-100 and ABR F4, the reduction is from 29.6 ± 0.3 to 12.8 ± 0.5 wt.% and from 29.6 ± 0.3 to 12.8 ± 0.5 wt.%, respectively, wt.%. At the same time, a new phase can be seen, identified as ytterbium garnet ($\text{Yb}_3\text{Al}_5\text{O}_{12}$, PDF card number 00-023-1476). This new phase was seen on the SEM images of the cross section, Fig. 6 and 8. The presence of garnet is most predominant on EBC SG-100, with a 7.0 ± 0.1 wt.%, whereas the two abrasible samples present a garnet phase content around or below 1 wt.%. This trend continues for the samples exposed at 1400 °C. EBC SG-100 experiences a further reduction in the YbMS content, down to 3.9 ± 0.4 wt.%, with garnet content rising to 17.6 ± 0.2 wt.%. Regarding ABR SG-100, exposure to steam at 1400 °C did increase the amount of garnet formed (2.6 ± 0.2 wt.%) compared to exposure at 1350 °C (0.1 ± 0.1 wt.%). This change is most notable in ABR F4, having a garnet content of 1.0 ± 0.1 wt.% when exposed at 1350 °C, rising to 7.2 ± 0.3 wt.% when exposed at 1400 °C. It should be noted that the phase content only takes into account the top 10–15 μm of the coatings due to the estimated penetration depth of x-rays for this composition (Ref 23).

The phase content as quantified through Rietveld refinement for all the samples here studied can be found in Fig. 11.

Discussion

Coating phase composition, microstructure, temperature and steam velocity (Ref 18) are some of the most common factors influencing the steam degradation of EBCs. In addition, the use of alumina tubes in steam rigs is a source of Al-containing impurities, which react with the coatings during testing, leading to the formation of garnet. Although this phenomenon has previously been reported in the literature (Ref 23–25), no previous work has studied the steam degradation of thermal-sprayed environmental barrier coatings with varying porosity levels, from traditional low porosity EBCs to higher porosity abrasible EBCs.

The three coatings studied here present a similar composition, as revealed by the XRD measurements in Fig. 5. EBC powder was mainly composed of YbDS, whereas

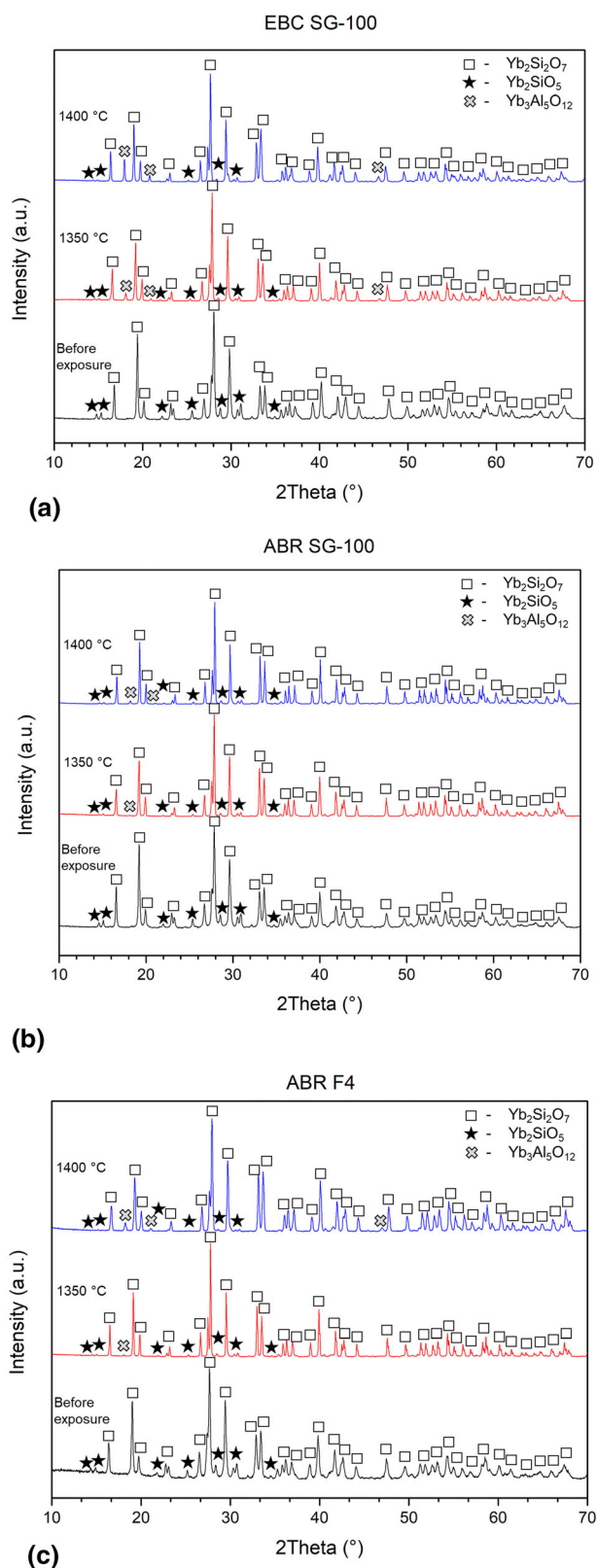


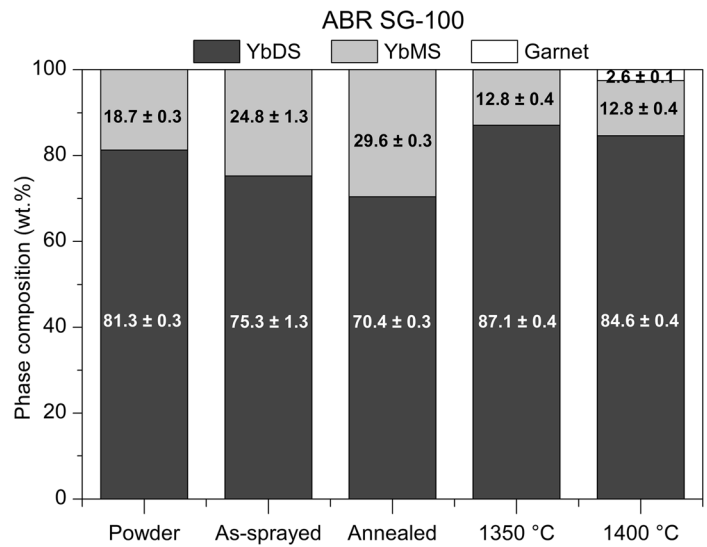
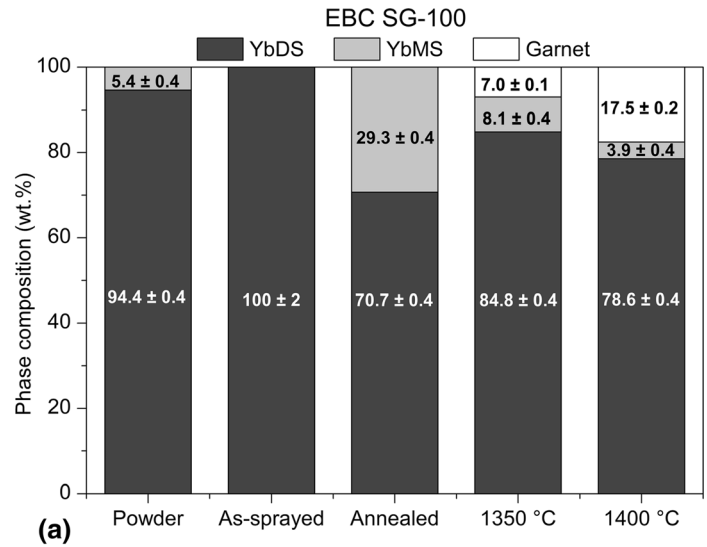
Fig. 10 XRD measurements for (a) EBC SG-100, (b) ABR SG-100 and (c) ABR F4. On each graph, bottom plot corresponds to the coating before steam exposure for 96 h, middle to the 1350 °C steam exposure and top to the 1400 °C steam exposure. Phases have been identified with a square (□) for YbDS, a star (★) for YbMS and a cross (×) for the garnet

ABR powder had traces of YbMS phase. During APS deposition, preferential volatilization of SiO_2 takes place due to the in-flight conditions, leading to the formation of small quantities of YbMS (Ref 45). This phase is in an amorphous state due to the rapid cooling experienced by the splats upon impact (Ref 46). This would explain why no distinguishable YbMS peaks can be found on the as-sprayed EBC SG-100 sample (Fig. 5a), where the amorphous content is as high as 63.6 %. Once the annealing treatment is completed, the amorphous content is crystallized, leading to only crystalline peaks for YbDS as the main phase and small quantities of YbMS.

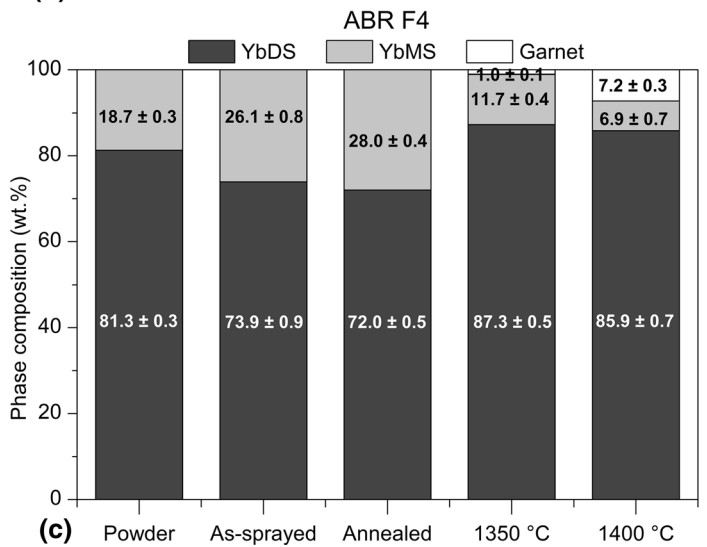
Despite this very similar starting composition of the annealed coatings, microstructure presents a differentiating factor between the EBC SG-100 sample and the two ABR coatings. As shown in the cross-sectional SEM images in Fig. 3, EBC SG-100 presented a lower porosity level ($2.4 \pm 0.3\%$) which can be explained by the absence of pores and defects in the feedstock powder as well as the lack of added polyester as pore former, as seen in Fig. 2(a). On the other hand, both the abrasible coatings, ABR SG-100 and ABR F4, present much higher levels of porosity, 21.3 ± 1.1 and $19.4 \pm 4.0\%$, respectively. These higher porosity levels are attributed to the presence of porosity and hollow cores in the feedstock powder, which generates more micropores in the coating structure (Fig. 2b), and to the addition of polyester as a pore former, which leads to the presence of some macropores on both abrasible coatings. When comparing the top surface of the annealed samples, there is also a clear difference between the EBC samples and the abrasible ones, as can be seen in Fig. 4. EBC SG-100 presents a smoother surface caused by well-molten splats that flattened upon impact. The abrasible samples show the presence of semi-molten, but not completely flat splats, giving rise to a rougher surface where individual splats are easily identifiable. In all of the three samples, intra- and inter-splat cracks could be found.

From the SEM images of the top surface of the three steam exposed coatings, shown in Fig. 7, it can be seen that the interaction between the steam (including the presence of gaseous Al-containing impurities) and the coatings takes place preferentially at the grain boundaries, a phenomenon also reported by Maier et al. (Ref 24) and Rohbeck et al. (Ref 25). Exposure to steam at 1350 °C caused the appearance of an YbMS depleted layer on all of the three

Fig. 11 Crystalline phase content quantified using Rietveld refinement for coatings EBC SG-100, ABR SG-100 and ABR F4. It should be noted that as-sprayed coatings are largely amorphous



(b)



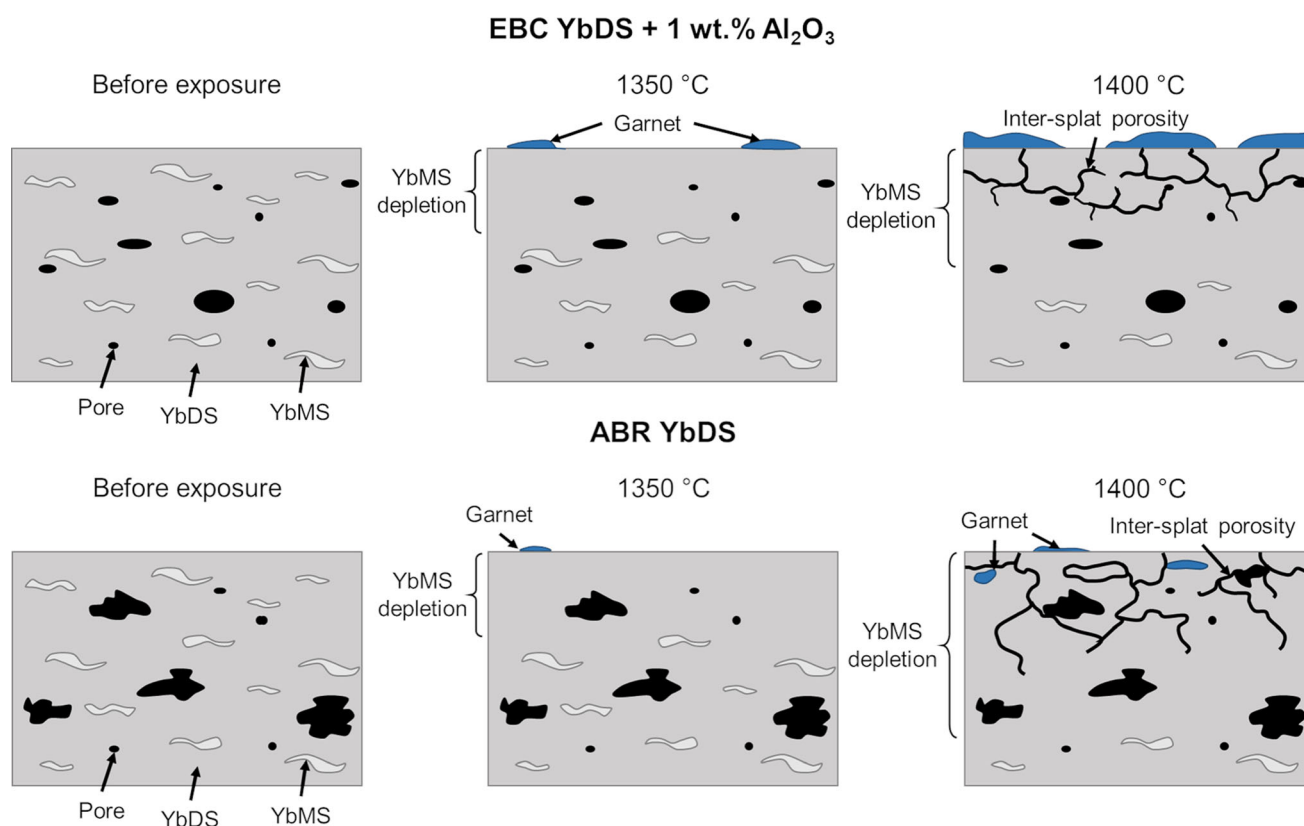
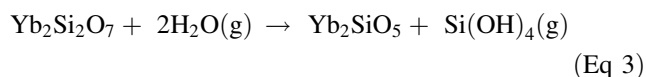


Fig. 12 Schematic with the different behavior of EBC YbDS + 1 wt.% Al₂O₃ and abradable YbDS coatings when exposed to steam at high temperature

coatings, as shown in Fig. 6, being particularly visible in the high magnification images. In addition to the depletion of YbMS from the top layers near the surface, XRD measurements indicate the formation of a new phase, identified as ytterbium garnet. Figure 11 shows the evolution of the quantitative phase content for each of the three coatings here studied. In all three coatings, a reduction in the YbMS content could be observed as the content of garnet increased.

Exposure of YbDS to flowing, high temperature steam has been reported to cause SiO₂ volatilization and YbMS formation through the reaction shown in Eq 3 (Ref 26, 34, 35, 39, 47, 48)



Nevertheless, in this work, no presence of an YbMS layer could be observed. Instead, a reduction in the YbMS content, including an YbMS depleted layer at the surface of the coatings, along with the appearance of garnet is detected. The appearance of garnet on steam exposure testing conducted using high purity alumina tubes is expected and has been extensively reported in the literature (23–25). In particular, Kane et al. (Ref 23) report the

formation of an YbMS depleted layer on a multilayer YbDS/Si EBC exposed to steam at 1300 °C. Their system, containing a Si bond coat, presented YbMS depletion both near the surface and at the Si-YbDS interface, suggesting the involvement of Si/SiO₂ in the YbMS depletion process, but they reported no presence of garnet at this temperature. As can be seen in Fig. 10, XRD measurements confirmed the presence of garnet at 1350 °C in all of the three samples, although sample EBC SG-100 showed the highest content. This seems to suggest two things: first, the formation of garnet is temperature dependent, with 1300 °C not high enough for the reaction to take place. Secondly, the 1 wt.% of alumina added to the feedstock EBC powder could explain why this sample shows the highest content of garnet at 1350 °C. Whereas the abradable samples rely on the Al-containing impurities from the furnace tubes to form the garnet via gas phase transport, the EBC SG-100 sample has the additional alumina within the coating.

Regarding the consumption of the YbMS phase to form garnet, similar results have been reported by Kane et al. (Ref 23) and Rohbeck et al. (Ref 25). Although Rohbeck et al. did not specify the steam velocity used in their experimental setup, Kane et al. measured their steam velocity to be 1.5 cm/s. It is suggested that steam velocity plays a key role in the corrosion mechanism observed (Ref

26), with low-velocity flowing steam not causing YbDS volatilization.

The mechanism behind the depletion of YbMS is not fully understood yet, although two mechanisms have been proposed in the literature. The first one involves the consumption of the YbMS as it reacts with the Al-containing impurities (or the alumina present within the coating in the case of sample EBC SG-100) to form the garnet phase. Kane et al. (Ref 23) suggested that YbMS is more reactive than YbDS regarding alumina, which would explain why YbDS is unaffected in the steam exposure. This mechanism is temperature dependent, as the lowest eutectic point of the Yb-Al-Si-O system is 1500 °C (Ref 49), although the presence of alkali impurities from the furnace may unlock the formation of aluminosilicate compounds at a lower temperature (Ref 23). This temperature dependence would explain the increase in YbMS depletion in all the samples in the 1400 °C steam exposure. When considering the 1400 °C exposure of sample EBC SG-100, it is worth noting that this sample was the one where the splat boundaries were more clearly visible, as presented in Fig. 8(b). For the two abradable coatings, this feature in the depleted layer was more difficult to detect due to the initial higher level of porosity. Similar to the infiltration of CMAS into YbDS (Ref 50-53), splat boundaries seem to be the preferential path for the ingress of Al-containing impurities, which would explain this phenomenon. Therefore, it can be suggested that this mechanism is prevalent in the case of sample EBC SG-100, where the extensive formation of garnet is observed. Once a dense scale of garnet is formed on the surface of the coating at 1400 °C, the ingress of Al-containing impurities is hindered, which slowed the expansion of the YbMS depleted layer compared to the abradable samples.

The second mechanism for the depletion of YbMS is based on the reaction between YbMS and SiO₂ to form YbDS. The presence of two YbMS depleted layers in work by Kane et al. (Ref 23), one near the surface and one near the Si bond coat after steam exposure at 1300 °C, supports the idea of a low temperature Si/SiO₂-mediated mechanism for the depletion of YbMS. The presence of SiO₂ could not be confirmed through XRD measurements, which could indicate that the quantity present is below the detection limit of the technique. The high content of ytterbium on the coatings limits the estimated x-ray penetration to below 10-15 μm (Ref 23), limiting the amount of SiO₂ available for detection. Additionally, the overlap between the YbMS and SiO₂ peaks might have masked the presence of traces amounts of SiO₂. Nevertheless, since the system here studied was a free-standing coating without the presence of a Si bond coat, and presence of SiO₂ could not be observed, this mechanism cannot be robustly argued to explain the phenomenon detected here. A schematic representing the

interaction between high-temperature steam and both EBC YbDS coating and abradable coatings is presented in Fig. 12.

From Fig. 12, it can be seen how EBC SG-100 presents depletion of YbMS once exposed to steam at 1350 °C, while forming small quantities of garnet located at the top surface due to the added alumina within the coating. At 1400 °C, the formation of garnet is more extensive, leading to a scale at the surface and a slightly larger depleted layer. Inter-splat boundaries can now be observed in the depleted layer, caused by the ingress of Al-containing contamination through these boundaries, consuming YbMS and forming garnet. In the case of the abradable samples, exposure to steam at 1350 °C also produces a YbMS depleted layer, although lower quantities of garnet are formed due to the absence of added alumina to the coatings. At 1400 °C, however, evidence of garnet formation can be observed, both at the surface and inside pores located near the surface. The depletion layer is considerably larger, containing also splat boundaries, along with larger pores. As previously mentioned, the presence of these inter-splat boundaries indicates that splat boundary is the preferential ingress path of gaseous Al-containing impurities.

Conclusions

Degradation of ytterbium disilicate EBCs under steam conditions is one of the main considerations for the successful implementation of SiC CMC components into the current generation of gas turbine engines. In this work, three free-standing YbDS coatings deposited using APS were exposed to steam at 1350 °C and 1400 °C for 96 h. The results show that sample EBC SG-100, with a low porosity level and 1 wt.% of Al₂O₃ added to the feedstock powder, presented moderate depletion of YbMS near the surface with the formation of ytterbium garnet. At 1400 °C, the garnet formed a dense scale at the surface and inter-splat boundaries were present within the YbMS depleted layer. The mechanism for the YbMS depletion is believed to be a reaction with gaseous Al-containing impurities from the alumina furnace tubes and the alumina present within the coating, leading to the formation of the garnet.

The two abradable samples, with 1.5 wt.% polyester added to the feedstock powder as a pore former, behaved in a similar fashion at 1350 °C, with the appearance of an YbMS depletion layer and traces amount of garnet detected. At 1400 °C, the size of the depleted layer grew considerably larger than in the case of the EBC sample, with less garnet phase forming. Porosity also increased within the depleted layer; however, its effect was more difficult to clearly identify due to the higher level of porosity. The

mechanism for the formation of the YbMS depleted layer is associated with the gaseous Al-containing impurities from the furnace. Since the abradable coatings did not contain added alumina, less garnet phase formed compared to the EBC coating.

In both cases, the exposure to flowing steam for 96 h at high temperature did not produce any evidence that the integrity of the coatings might be compromised, both in terms of cracking or loss of mass. Nevertheless, Al-containing impurities coming from the furnace tubes played a key role in the steam degradation of the coatings, requiring further investigation using experimental setups where external contributions are not a factor.

Acknowledgment This work was supported by the Engineering and Physical Sciences Research Council (EPSRC) (grant number EP/L016206/1). The authors would like to thank Dr Hannah Constantin for her assistance in performing the XRD measurements and to the Nanoscale and Microscale Research Centre (nmRC) for providing access to instrumentation.

Data Availability Data subject to third party restrictions. The data that support the findings of this study are available from Rolls-Royce plc. (Derby, UK) but restrictions apply to the availability of these data, which were used under license for the current study, and so are not publicly available. Data are, however, available from the authors upon reasonable request and with permission of Rolls-Royce plc. (Derby, UK).

Conflict of interest The authors declare that they have no conflict of interest.

Open Access This article is licensed under a Creative Commons Attribution 4.0 International License, which permits use, sharing, adaptation, distribution and reproduction in any medium or format, as long as you give appropriate credit to the original author(s) and the source, provide a link to the Creative Commons licence, and indicate if changes were made. The images or other third party material in this article are included in the article's Creative Commons licence, unless indicated otherwise in a credit line to the material. If material is not included in the article's Creative Commons licence and your intended use is not permitted by statutory regulation or exceeds the permitted use, you will need to obtain permission directly from the copyright holder. To view a copy of this licence, visit <http://creativecommons.org/licenses/by/4.0/>.

References

1. N.P. Padture, Advanced Structural Ceramics in Aerospace Propulsion, *Nat. Mater.*, 2016, **15**(8), p 804-809.
2. M. van Roode, Ceramic Gas Turbine Development: Need for a 10Year Plan, *J. Eng. Gas Turb. Power*, 2009, **132**(1)
3. J. Steibel, Ceramic Matrix Composites Taking Flight at GE Aviation, *Am. Ceram. Soc. Bull.*, 2019, **98**(3), p 30-33.
4. K.M. Grant, S. Krämer, J.P. Löfvander, and C.G. Levi, CMAS Degradation of Environmental Barrier Coatings, *Surf. Coat. Technol.*, 2007, **202**(4-7), p 653-657.
5. K.M. Grant, S. Krämer, G.G.E. Seward, and C.G. Levi, Calcium-Magnesium Alumino-Silicate Interaction with Yttrium Monosilicate Environmental Barrier Coatings, *J. Am. Ceram. Soc.*, 2010, **93**(10), p 3504-3511.
6. D.L. Poerschke, D.D. Hass, S. Eustis, G.G.E. Seward, J.S. Van Sluhtman, and C.G. Levi, Stability and CMAS Resistance of Ytterbium-Silicate/Hafnate EBCs/TBC for SiC Composites, *J. Am. Ceram. Soc.*, 2015, **98**(1), p 278-286.
7. N.S. Jacobson, J.L. Smialek, and D.S. Fox, Molten Salt Corrosion of SiC and Si₃N₄, *Handbook of Ceramics and Composites*. CRC Press, Boca Raton, 2021, p 99-136
8. J. Kim, M. Dunn, A. Baran, D. Wade, and E. Tremba, Deposition of Volcanic Materials in the Hot Sections of Two Gas Turbine Engines, In: Turbo Expo: Power for Land, Sea, and Air, 1992, American Society of Mechanical Engineers, p V003T005A001
9. N. Al Nasiri, N. Patra, N. Ni, D.D. Jayaseelan, and W.E. Lee, Oxidation Behaviour of SiC/SiC Ceramic Matrix Composites in Air, *J. Eur. Ceram. Soc.*, 2016, **36**(14), p 3293-3302.
10. E.J. Opila and R.E. Hann Jr., Paralineer Oxidation of CVD SiC in Water Vapor, *J. Am. Ceram. Soc.*, 1997, **80**(1), p 197-205.
11. N.S. Jacobson, Corrosion of Silicon-Based Ceramics in Combustion Environments, *J. Am. Ceram. Soc.*, 1993, **76**(1), p 3-28.
12. E.J. Opila, Variation of the Oxidation Rate of Silicon Carbide with Water-Vapor Pressure, *J. Am. Ceram. Soc.*, 1999, **82**(3), p 625-636.
13. E.J. Opila, Oxidation Kinetics of Chemically Vapor-Deposited Silicon Carbide in Wet Oxygen, *J. Am. Ceram. Soc.*, 1994, **77**(3), p 730-736.
14. K. Kane, E. Garcia, P. Stack, M. Lance, C. Parker, S. Sampath, and B.A. Pint, Evaluating Steam Oxidation Kinetics of Environmental Barrier Coatings, *J. Am. Ceram. Soc.*, 2022, **105**(1), p 590-605.
15. E.J. Opila, D.S. Fox, and N.S. Jacobson, Mass Spectrometric Identification of Si-O-H (g) Species from the Reaction of Silica with Water Vapor at Atmospheric Pressure, *J. Am. Ceram. Soc.*, 1997, **80**(4), p 1009-1012.
16. S.L. dos Santos e Lucato, O.H. Sudre, and D.B. Marshall, A Method for Assessing Reactions of Water Vapor with Materials in High-Speed, High-Temperature Flow, *J. Am. Ceram. Soc.*, 2011, **94**, p s186-s195.
17. E.J. Opila, J.L. Smialek, R.C. Robinson, D.S. Fox, and N.S. Jacobson, SiC Recession Caused by SiO₂ Scale Volatility Under Combustion conditions: II, Thermodynamics and Gaseous-Diffusion Model, *J. Am. Ceram. Soc.*, 1999, **82**(7), p 1826-1834.
18. D. Tejero-Martin, C. Bennett, and T. Hussain, A Review on Environmental Barrier Coatings: History, Current State of the Art and Future Developments, *J. Eur. Ceram. Soc.*, 2021, **41**(3), p 1747-1768.
19. A.J. Fernández-Carrión, M. Allix, and A.I. Becerro, Thermal Expansion of Rare-Earth Pyrosilicates, *J. Am. Ceram. Soc.*, 2013, **96**(7), p 2298-2305.
20. Y. Xu, X. Hu, F. Xu, and K. Li, Rare Earth Silicate Environmental Barrier Coatings: Present Status and Prospective, *Ceram. Int.*, 2017, **43**(8), p 5847-5855.
21. J. Felsche, The Crystal Chemistry of the Rare-Earth Silicates, *Rare Earths*. Springer, Berlin, Heidelberg, 1973, p 99-197
22. L.R. Turcer and N.P. Padture, Towards Multifunctional Thermal Environmental Barrier Coatings (TEBCs) Based on Rare-Earth Pyrosilicate Solid-Solution Ceramics, *Scripta Mater.*, 2018, **154**, p 111-117.
23. K.A. Kane, E. Garcia, S. Uwanyuze, M. Lance, K.A. Unocic, S. Sampath, and B.A. Pint, Steam Oxidation of Ytterbium Disilicate Environmental Barrier Coatings with and without a Silicon Bond Coat, *J. Am. Ceram. Soc.*, 2021, **104**(5), p 2285-2300.
24. N. Maier, K. Nickel, and G. Rixecker, High Temperature Water Vapour Corrosion of Rare Earth Disilicates (Y, Yb, Lu) 2Si₂O₇ in the Presence of Al (OH) ₃ Impurities, *J. Eur. Ceram. Soc.*, 2007, **27**(7), p 2705-2713.

25. N. Rohbeck, P. Morrell, and P. Xiao, Degradation of Ytterbium Disilicate Environmental Barrier Coatings in High Temperature Steam Atmosphere, *J. Eur. Ceram. Soc.*, 2019, **39**(10), p 3153-3163.
26. M. Ridley and E. Opila, Thermochemical Stability and Microstructural Evolution of Yb₂Si₂O₇ in High-Velocity High-Temperature Water Vapor, *J. Eur. Ceram. Soc.*, 2021, **41**(5), p 3141-3149.
27. S. Ueno, D.D. Jayaseelan, and T. Ohji, Development of Oxide-Based EBC for Silicon Nitride, *Int. J. Appl. Ceram. Technol.*, 2004, **1**(4), p 362-373.
28. K.N. Lee, D.S. Fox, and N.P. Bansal, Rare Earth Silicate Environmental Barrier Coatings for SiC/SiC Composites and Si₃N₄ Ceramics, *J. Eur. Ceram. Soc.*, 2005, **25**(10), p 1705-1715.
29. G.C. Costa and N.S. Jacobson, Mass Spectrometric Measurements of the Silica Activity in the Yb₂O₃-SiO₂ System and Implications to Assess the Degradation of Silicate-Based Coatings in Combustion Environments, *J. Eur. Ceram. Soc.*, 2015, **35**(15), p 4259-4267.
30. N. Al Nasiri, N. Patra, D. Jayaseelan, and W. Lee, Water Vapour Corrosion of Rare Earth Monosilicates for Environmental Barrier Coating Application, *Ceram. Int.*, 2017, **43**(10), p 7393-7400.
31. S. Ueno, D.D. Jayaseelan, H. Kita, T. Ohji, and H.T. Lin, Comparison of Water Vapor Corrosion Behaviors of Ln₂Si₂O₇ (Ln= Yb and Lu) and ASiO₄ (A= Ti, Zr and Hf) EBC's, *Key Eng. Mater.*, 2006, **317**, p 557-560.
32. P. Mechnich, Y₂SiO₅ Coatings Fabricated by RF Magnetron Sputtering, *Surf. Coat. Technol.*, 2013, **237**, p 88-94.
33. N. Al Nasiri, N. Patra, M. Pezoldt, J. Colas, and W. Lee, Investigation of a Single-Layer EBC Deposited on SiC/SiC CMCs: Processing and Corrosion Behaviour in High-Temperature steam, *J. Eur. Ceram. Soc.*, 2019, **39**(8), p 2703-2711.
34. E. Bakan, Y.J. Sohn, W. Kunz, H. Klemm, and R. Vaßen, Effect of Processing on High-Velocity Water Vapor Recession Behavior of Yb-Silicate Environmental Barrier Coatings, *J. Eur. Ceram. Soc.*, 2019, **39**(4), p 1507-1513.
35. E. Bakan, M. Kindelmann, W. Kunz, H. Klemm, and R. Vaßen, High-Velocity Water Vapor Corrosion of Yb-Silicate: Sprayed vs. Sintered Body, *Scripta Mater.*, 2020, **178**, p 468-471.
36. E. Bakan, D. Marcano, D. Zhou, Y.J. Sohn, G. Mauer, and R. Vaßen, Yb₂Si₂O₇ Environmental Barrier Coatings Deposited by Various Thermal Spray Techniques: A Preliminary Comparative Study, *J. Therm. Spray Technol.*, 2017, **26**(6), p 1011-1024.
37. D. Qin, Y. Niu, H. Li, X. Zhong, X. Zheng, and J. Sun, Fabrication and Characterization of Yb₂Si₂O₇-Based Composites as Novel Abradable Sealing Coatings, *Ceram. Int.*, 2021, **47**(16), p 23153-23161.
38. A.H. Paksoy, J.F. Martins, H. Cao, Y. Chen, G. Gibson, and P. Xiao, Influence of Alumina Addition on Steam Corrosion Behaviour of Ytterbium Disilicates for Environmental Barrier Coating Applications, *Corros. Sci.*, 2022, **207**, p 110555.
39. B.T. Richards, K.A. Young, F. de Francqueville, S. Sehr, M.R. Begley, and H.N. Wadley, Response of Ytterbium Disilicate-Silicon Environmental Barrier Coatings to Thermal Cycling in Water Vapor, *Acta Mater.*, 2016, **106**, p 1-14.
40. P. Scardi and M. Leoni, Whole Powder Pattern Modelling, *Acta Crystallogr. Sect. A Found. Crystallogr.*, 2002, **58**(2), p 190-200.
41. J. Schindelin, I. Arganda-Carreras, E. Frise, V. Kaynig, M. Longair, T. Pietzsch, S. Preibisch, C. Rueden, S. Saalfeld, and B. Schmid, Fiji: An Open-Source Platform for Biological-Image Analysis, *Nat. Methods*, 2012, **9**(7), p 676-682.
42. D. Tejero-Martin, A.R. Romero, R.G. Wellman, and T. Hussain, Interaction of CMAS on Thermal Sprayed Ytterbium Disilicate Environmental Barrier Coatings: A Story of Porosity, *Ceram. Int.*, 2022, **48**(6), p 8286-8296.
43. D. Aussavy, R. Bolot, G. Montavon, F. Peyraud, G. Szyndelman, J. Gurt-Santanach, and S. Selezneff, YSZ-Polyester Abradable Coatings Manufactured by APS, *J. Therm. Spray Technol.*, 2016, **25**(1), p 252-263.
44. V. Fournier, A. Quet, E. Meillot, and H. Ageorges, Plasma Spraying of Mullite and Pore Formers for Thermal Insulating Applications, *Surf. Coat. Technol.*, 2021, **406**, p 126744.
45. E. Garcia, O. Sotelo-Mazon, C. Poblano-Salas, G. Trapaga, and S. Sampath, Characterization of Yb₂Si₂O₇-Yb₂SiO₅ Composite Environmental Barrier Coatings Resultant from in situ Plasma Spray Processing, *Ceram. Int.*, 2020, **46**(13), p 21328-21335.
46. S.A. Sampath and H. Herman, Rapid Solidification and Microstructure Development During Plasma Spray Deposition, *J. Therm. Spray Technol.*, 1996, **5**(4), p 445-456.
47. S. Ueno, T. Ohji, and H.-T. Lin, Recession Behavior of Yb₂Si₂O₇ Phase Under High Speed Steam Jet at High Temperatures, *Corros. Sci.*, 2008, **50**(1), p 178-182.
48. E. Bakan, D.E. Mack, S. Lobe, D. Koch, and R. Vaßen, An Investigation on Burner Rig Testing of Environmental Barrier Coatings for Aerospace Applications, *J. Eur. Ceram. Soc.*, 2020, **40**(15), p 6236-6240.
49. Y. Murakami and H. Yamamoto, Phase-Equilibria and Properties of Glasses in the Al₂O₃-Yb₂O₃-SiO₂ System, *Nippon Seramikkusu Kyokai Gakujutsu Ronbunshi-J. Ceram. Soc. Japan*, 1993, **101**(10), p 1101-1106.
50. L.R. Turcer, A.R. Krause, H.F. Garces, L. Zhang, and N.P. Padture, Environmental-Barrier Coating Ceramics for Resistance Against Attack by Molten Calcia-Magnesia-Aluminosilicate (CMAS) Glass: Part I, YAIO₃ and γ -Y₂Si₂O₇, *J. Eur. Ceram. Soc.*, 2018, **38**(11), p 3905-3913.
51. J.L. Stokes, B.J. Harder, V.L. Wiesner, and D.E. Wolfe, High-Temperature Thermochemical Interactions of Molten Silicates with Yb₂Si₂O₇ and Y₂Si₂O₇ Environmental Barrier Coating Materials, *J. Eur. Ceram. Soc.*, 2019, **39**(15), p 5059-5067.
52. J. Liu, L. Zhang, Q. Liu, L. Cheng, and Y. Wang, Calcium-Magnesium-Aluminosilicate Corrosion Behaviors of Rare-Earth Disilicates at 1400 °C, *J. Eur. Ceram. Soc.*, 2013, **33**(15-16), p 3419-3428.
53. F. Stolzenburg, M. Johnson, K. Lee, N. Jacobson, and K. Faber, The Interaction of Calcium-Magnesium-Aluminosilicate with Ytterbium Silicate Environmental Barrier Materials, *Surf. Coat. Technol.*, 2015, **284**, p 44-50.

Publisher's Note Springer Nature remains neutral with regard to jurisdictional claims in published maps and institutional affiliations.